GR JOURNALS

Journal of Collective Sciences and Sustainability

Research Article | *Open Access* |

Development of Electric Field-Controlled Open-System Ionic Thruster

Shaik Aadil Iftikhaar* Pritee Parwekar and Md. Akhtar Khan

School of Technology, GITAM University, GITAM Deemed to be University, Hyderabad, Telangana, 502329, India
**Email:* ashaik39@gitam.in (A. I. Shaik)

Abstract

This study presents the development of an open-system ionic thruster designed for silent and efficient propulsion under atmospheric conditions. The thruster operates by generating a high-voltage corona discharge that ionizes a working medium, either ambient air or a noble gas such as argon, and accelerates the resulting ions using a controlled electrostatic field. The thrust is produced by the momentum transfer of these ions as they are expelled from the system. A key focus of the design is the geometry of the negative (collector) electrode, which is shaped to manipulate the local electric field and maximize ion acceleration while minimizing energy loss and ion recombination. The proposed system offers a mechanically simple, scalable and modular solution without moving parts, making it ideal for applications requiring silent operation and precise thrust control, such as unmanned aerial vehicles, near-space platforms, and experimental aerospace propulsion systems.

***Keywords*:** Silent; No moving parts; Open system; Field manipulation; Corrona discharge; Precise thrust; Modular.

Received: 05 May 2025; Revised: 12 June 2025; Accepted: 23 June 2025; Published Online: 25 June 2025.

1. Introduction

Ionic propulsion is an electrostatic method of thrust generation that uses electric fields to accelerate charged particles. Unlike conventional propulsion systems with moving parts and combustion, ionic thrusters operate silently by ionizing a working medium and directing the ions to produce thrust. The principle involves generating a corona discharge between two electrodes. This discharge ionizes air or gas molecules, typically forming positive ions that are then accelerated by an electric field. Fig. 4 demonstrates an early prototype implementation of this principle, showing the fundamental electrode configuration used for ion acceleration.

Although ionic propulsion has been primarily used in space applications under vacuum conditions, recent studies have demonstrated its feasibility in atmospheric environments. However, atmospheric operation presents challenges such as increased ion recombination, energy losses, and reduced efficiency.

This study focuses on developing an open-system ionic thruster that operates in ambient air. The final optimized designs, shown in Figs. 1 and 2, represent the culmination of iterative geometric refinements aimed at maximizing thrust efficiency while maintaining silent operation.

1.1 Related work – technical comparative analysis

1.1.1 MIT ionic wind plane – Electro-aerodynamic Propulsion (EAD)

The MIT EAD prototype demonstrates a solid-state propulsion system that utilizes high-voltage (20–40 kV) corona discharge to ionize air molecules, primarily N_2^+ and O_2^+. The ions are accelerated towards a downstream collector electrode, and their momentum is transferred to neutral air molecules through ion-neutral collisions. This produces a net thrust commonly referred to as ionic wind. Notably, this process occurs in weakly ionized air at atmospheric pressure without forming plasma.[1]

It features a completely solid-state and silent design with

DOI: https://doi.org/10.64189/css.25406

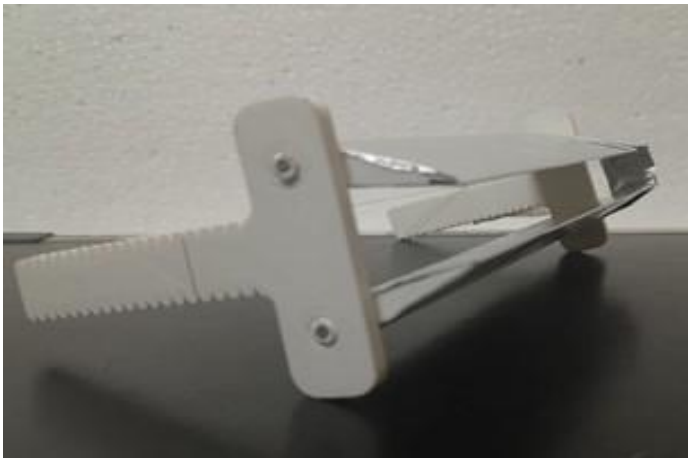

Fig. 1: Iterated model with optimised electrode.

no moving parts, and it operates in ambient air without requiring onboard propellant. However, its performance scales poorly with altitude due to reduced atmospheric density. In contrast, our proposed open-system design (Fig. 1 and Fig. 2) addresses this limitation through optimized electrode geometry that maintains efficiency across varying atmospheric conditions.

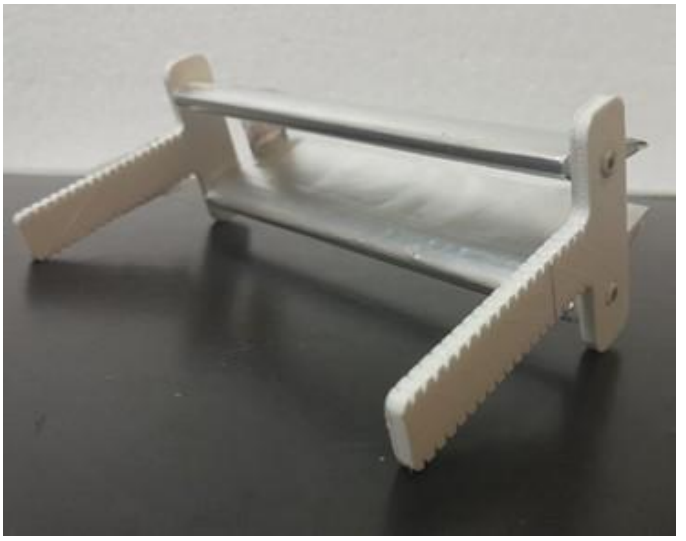

Fig. 2: Iterated model with optimise electrode.

Applications include low-altitude drones, experimental UAVs, and lightweight surveillance systems. The prototype achieved a thrust-to-power ratio of approximately 0.6 mN/W, with a flight duration of around 12 seconds over 60 meters.[1] The prototype achieved a thrust-to-power ratio of approximately 0.6 mN/W. Our experimental setup, shown in Fig. 3, demonstrates comparable thrust generation capabilities.

1.1.2 NASA Hall Effect Thruster (HET)

The Hall Effect Thruster employed by NASA functions by trapping electrons in a radial magnetic field, which results in a Hall current that ionizes xenon propellant. The generated plasma is accelerated axially by an electric field, producing thrust via the Lorentz force.[2]

The system is efficient, using either permanent magnets or electromagnets to optimize the field configuration. It performs optimally in vacuum conditions, making it suitable for deep space missions such as Psyche and DART, as well as satellite station-keeping in geostationary and low Earth orbit.

Typical performance includes a specific impulse between 1,600–2,700 seconds and an efficiency of 50–60%, with thrust outputs ranging from 40–200 mN depending on the model.[2,3]

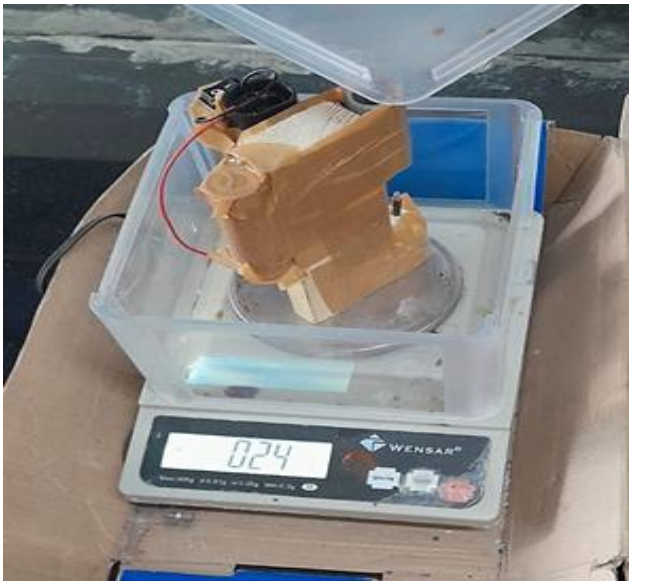

Fig. 3: Experimental prototype showing thrust in grams.

1.1.3 ISRO Gridded Ion Thruster (XIPS-Type)

ISRO's ion thruster is based on a xenon ion propulsion system similar to the XIPS architecture. It ionizes xenon gas using a hot filament cathode inside a cylindrical discharge chamber. The ions are extracted and accelerated through multiple electrostatic grid stages, while a downstream neutralizer ensures charge balance.[4]

The design is tailored for geostationary satellite station-keeping and offers long operational life exceeding 10,000 hours. It has been implemented in the GSAT satellite series and evaluated for interplanetary mission applications.

The thruster exhibits a specific impulse of around 3,000 seconds, a thrust of 25–35 mN, and an efficiency of approximately 60%.[4]

1.1.4 Busek Co. – BHT series hall effect thrusters

The BHT series from Busek Co. follows the traditional Hall-effect mechanism, using a radial magnetic field within an annular discharge channel. Innovations include boron nitride ceramic insulators, scalable chamber architecture, and power adaptability, allowing deployment across different spacecraft classes.[5]

These thrusters have flown on CubeSats (e.g., BHT-200) and large spacecraft platforms (e.g., BHT-6000), including missions such as STPSat-4 and AFRL programs. Applications span orbital station-keeping, interplanetary

probes, and broadband satellite constellations like OneWeb. For instance, the BHT-6000 model delivers a thrust of 270–340 mN with a power input of 6 kW and a specific impulse up to 2,300 seconds.[5,6]

1.1.5 Aerojet Rocketdyne – AEPS (Advanced Electric Propulsion System)

AEPS utilizes radio-frequency (RF) excitation to generate plasma in a cylindrical chamber, followed by ion acceleration through multi-stage electrostatic grids. Beam neutralization is achieved using a cathode at the exit plane. The system is designed for high-power deep-space missions.[7]

It supports high voltage grids (6–8 kV) and includes redundant control electronics for reliability in long-duration missions. AEPS has been selected for use in NASA's Artemis and Lunar Gateway programs.

Performance-wise, the system delivers thrust around 200–250 mN, with a power requirement of approximately 12–13 kW and a specific impulse near 3,400 seconds.[7,8]

1.1.6 Frore Systems – AirJet® solid-state ionic cooling

Frore Systems' AirJet® technology applies ionic wind principles to the domain of thermal management. It uses MEMS-based high-voltage drivers that ionize ambient air via corona discharge. The ions are driven across narrow electrode gaps to produce airflow by electrohydrodynamic drift, eliminating the need for mechanical fans.[9]

The system operates at high-frequency field oscillations (20–40 kHz) and is exceptionally thin (less than 3 mm), making it suitable for ultra-compact electronic devices. Applications include passive or hybrid cooling in consumer electronics, such as high-performance laptops, GPUs, and CPUs.

Performance includes up to 5.25 CFM airflow, around 1750 Pa static pressure, and a low noise level of 21 dBA, offering near-silent cooling performance.[9,10]

1.2 Research gap

Despite the advancement of ionic propulsion systems, there are several unresolved challenges that hinder their broader adoption and performance scalability.A primary concern is scalability. High-power Hall effect thrusters, such as NASA's 457M v2, display a nonlinear decrease in efficiency at higher power levels. The thrust-to-power ratio drops from 76.4 mN/kW at low input power to just 46.1 mN/kW at 50 kW, indicating nonlinear scaling inefficiencies. The modular architecture demonstrated in Fig. 1 and 2 addresses this limitation by enabling linear thrust scaling through geometric extension rather than power increase. On the other end of the spectrum, miniaturization efforts for CubeSats and small satellites face limitations such as plasma confinement losses and rapid electrode erosion. These arise because of reduced mean free paths and enhanced wall interactions in microdischarge regimes, making effective downscaling a difficult engineering task.

Propellant limitations also pose major constraints. Xenon, the most commonly used propellant, is both expensive and logistically complex. Its price ranges from $5,000 to $12,000 per kilogram, and it must be stored under high pressure, adding weight and complexity to spacecraft designs. Alternatives like krypton and argon are cheaper but offer lower performance and pose integration difficulties in existing systems that are optimized for xenon.

Environmental adaptability is another major challenge. Systems like the MIT electro-aerodynamic aircraft are only effective below altitudes of 2 kilometers, due to the significant drop in ionization efficiency at lower atmospheric pressures. In contrast, traditional ion engines are designed to operate in high vacuum and cannot function effectively in transitional pressure environments such as near-space or low-atmosphere zones. This creates a technological gap between Earth-based and space-based ion propulsion capabilities.

Magnetic field precision is critical in systems like Hall effect thrusters. These rely on carefully tuned radial magnetic fields to trap electrons and form stable plasmas. Slight deviations in the magnetic configuration can drastically affect thrust efficiency. Furthermore, magnetic components are vulnerable to thermal saturation and demagnetization under high operational temperatures, which can degrade performance over time or under continuous operation.

Another significant technical issue is ion beam divergence and recombination losses. Beams from ion engines typically diverge by 10° to 30°, which causes a loss in axial thrust and raises the risk of contaminating nearby spacecraft surfaces. The comparative field simulations shown in Fig. 5 and Fig. 6 illustrate how different electrode geometries can either exacerbate or mitigate these losses, with open curved configurations (Fig. 6) showing superior ion guidance compared to closed profiles (Fig. 5). Additionally, sheath instabilities near the extraction grids can lead to ion recombination, reducing propulsion efficiency by as much as 15 to 25 percent.

Finally, ionic propulsion systems continue to struggle with low thrust-to-power ratios. Hall thrusters generally deliver between 50 to 60 mN per kilowatt, a figure too low for missions requiring rapid acceleration or agile orbital maneuvers. This limits their use to slow and gradual trajectory adjustments or deep space cruise operations rather than dynamic or tactical applications.

2. Proposed methodology

The objective is to develop a modular, open-system ionic thruster that eliminates the reliance on magnetic field guidance by instead engineering the topology of the negative electrode to control ion trajectories, minimize recombination, and shape the electric field effectively. This concept leverages electrostatic-only field manipulation to direct positive ions, reducing system complexity and thermal

sensitivity associated with traditional magnetic configurations.[2]

The thruster architecture utilizes a corona wire or thin emitter as the positively charged ionization electrode, paired with a negatively charged collector electrode whose curvature and edge geometry are carefully designed to steer electric field lines. The optimized electrode configurations shown in Fig. 1 and Fig. 2 demonstrate how geometric refinements can enhance ion flow direction and minimize energy losses. This method allows precise ion acceleration in the desired direction, while avoiding the need for magnetic trapping or shielding mechanisms. Fig. 5 illustrates the field confinement achievable with closed electrode geometries, while Fig. 6 demonstrates the enhanced ion throughput possible with optimized open configurations.[3] By optimizing the electrode geometry, recombination zones and field divergence are minimized, thus improving thrust efficiency and ensuring consistent particle ejection.[4]

In contrast to enclosed thruster systems like Hall or gridded ion engines, this design adopts an open structural layout. In atmospheric conditions, the open geometry naturally facilitates passive intake of ambient air via Bernoulli-driven inflow. The air is ionized as it moves through the electric field region, enabling entrainment of neutral particles into the ion stream and enhancing net thrust. This passive intake mechanism removes the need for auxiliary compressors or pumps and is particularly well-suited for silent, low-maintenance operation in drone or UAV platforms.[9]

Scalability is achieved through proportional extension of the electrode length. While the ion acceleration path (and hence exhaust velocity) remains constant—being determined solely by the applied voltage—the total ionized mass flow increases with surface area. This allows the thrust output to scale linearly without affecting the core propulsion dynamics. Unlike conventional designs that suffer from nonlinear scaling inefficiencies at high input powers,[3] this architecture maintains consistent performance across size classes.

The modular nature of this design further allows integration of multiple thruster units along the structural skin of a vehicle or satellite. Each unit operates independently and can be selectively activated, enabling distributed thrust vectoring, redundancy, and fault tolerance.[10] This is particularly advantageous for platforms requiring directional control without mechanical actuators, and for spacecraft or drones operating in environments with limited access for repair.

Compared to magnetic and closed-chamber systems, the proposed approach reduces system mass, complexity, and manufacturing costs. It eliminates the need for high-pressure gas storage, magnetic shielding, or grid alignment tolerances found in traditional gridded ion thrusters.[6] The entire propulsion process—from ion generation to acceleration-relies purely on electrostatics, making it ideal for low-power missions. This principle is validated through the experimental prototype shown in Fig. 4, which demonstrates functional ion acceleration using minimal infrastructure, making it ideal for low-power missions, particularly in micro-UAVs, nanosatellites, and experimental solid-state aircraft. Furthermore, its dual-mode compatibility with both atmospheric and vacuum conditions increases deployment versatility, potentially enabling multi-phase operation from launch to space transition.[7]

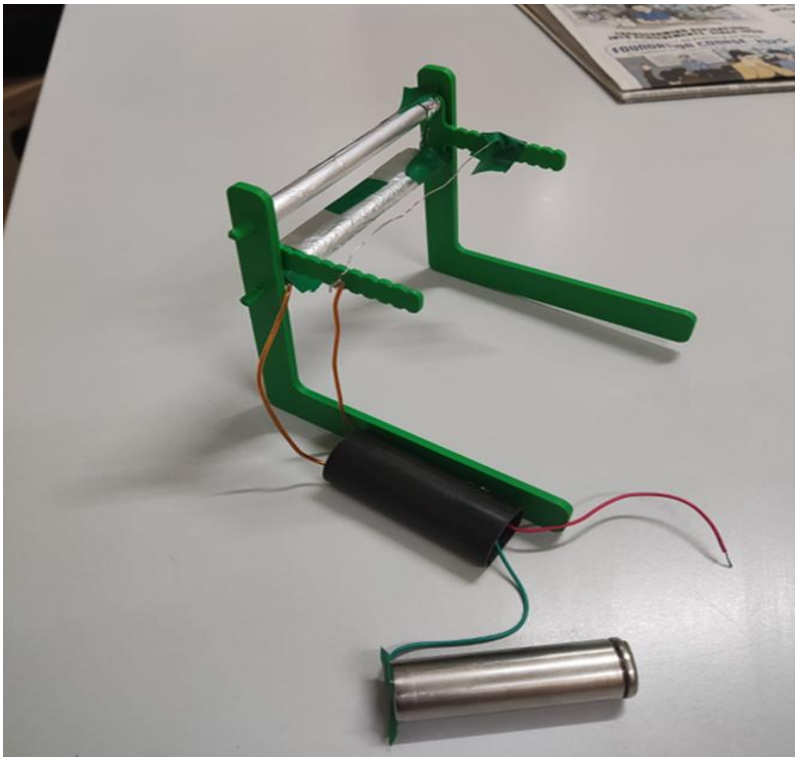

Fig. 4: First prototype testing of electrode modification.

3. Implementation

3.1 Stage 1: Electric field modeling

3.1.1 Electric field of a point charge

At a point $\vec{r}=(x,y)$ due to a charge q_i at position $\vec{r}_i=(x_i,y_i)$:

$$\vec{E}_i(\vec{r})=\frac{1}{4\pi\varepsilon_0}\cdot\frac{q_i(\vec{r}-\vec{r}_i)}{|\vec{r}-\vec{r}_i|^3} \quad (1)$$

where,
$\vec{r}=(x,y)$ is the observation point in 2D space,
$\vec{r}_i=(x_i,y_i)$ is the position of the source charge q_i,
$\varepsilon_0=8.854\times10^{-12}$ F/m is the vacuum permittivity,
$\vec{E}_i$ is the electric field at $\vec{r}$ due to q_i,
$\vec{E}_{net}=\sum_i\vec{E}_i$ is the net electric field from all point charges.
This formulation is fundamental for computing the superposed field distribution from discrete charges—essential in understanding field shaping around electrodes. The practical applications of these calculations are demonstrated in Fig. 5 and Fig. 6, which show how different electrode geometries produce distinct field patterns and ion trajectories.

3.1.2 Minimum radius of curvature

For a cylindrical conductor or electrode with radius of curvature r, the electric field at its surface due to a potential difference V is approximately:

$$E=\frac{V}{r\cdot\ln\left(\frac{2h}{r}\right)} \quad (2)$$

where,
E is the electric field intensity at the conductor surface,
V is the potential difference between the electrode and its reference (e.g., ground),
r is the radius of curvature at the conductor tip,
h is the distance from the conductor to the ground plane or opposing electrode.
This relation provides a practical way to estimate field concentration at sharp points—critical for predicting corona onset regions.

3.1.3 Simulation methodology

a) Initialize 2D Grid
Create a meshgrid of points over the defined range using:

$$X,Y=\text{meshgrid}(x,y) \quad (3)$$

where,
$x\in[x_{min},x_{max}]$ and $y\in[y_{min},y_{max}]$ define the spatial simulation bounds,
X and Y represent the grid coordinates of each point in the 2D plane.
b) Initialize fields:

$$E_x(x,y)=0,\quad E_y(x,y)=0 \quad (4)$$

where,
E_x and E_y are the x and y components of the electric field at each grid point.
c) Loop over all charges
For each charge (x_i,y_i,q_i):
Compute displacement:

$$dx=X-x_i,\quad dy=Y-y_i \quad (5)$$

where,
dx and dy are component-wise differences between grid points and the charge location.
Compute distance:

$$r^2=dx^2+dy^2,\quad r=\sqrt{r^2} \quad (6)$$

where,
r^2 is the squared distance from the charge to a grid point,
r is the Euclidean distance, used in field decay calculations.
Apply mask to avoid division by zero:

$$\text{mask}=r>\epsilon \quad (7)$$

where,
ϵ is a small positive constant to exclude singularities (e.g., 10^{-6} m).
Compute field components (only where mask is True):

$$E_{x_i}=k\cdot q_i\cdot\frac{dx}{r^3},\quad E_{y_i}=k\cdot q_i\cdot\frac{dy}{r^3} \quad (8)$$

where,
$k=\frac{1}{4\pi\varepsilon_0}$ is Coulomb's constant,
q_i is the charge value,
E_{x_i},E_{y_i} are the field components at each point.
Accumulate:

$$E_x+=E_{x_i},\quad E_y+=E_{y_i} \quad (9)$$

which adds the contribution of each charge to the total field.
d) Compute field magnitude:

$$E_{magnitude}=\sqrt{E_x^2+E_y^2} \quad (10)$$

where,
$E_{magnitude}$ is the scalar field strength at each grid point—useful for visualizing field peaks.
e) Normalize direction vectors (for uniform arrow length):

$$E_{x\_norm}=\frac{E_x}{E_{magnitude}+\delta},\quad E_{y\_norm}=\frac{E_y}{E_{magnitude}+\delta} \quad (11)$$

where:
δ is a small stabilizer to avoid division by zero,
E_{x_norm},E_{y_norm} are unit direction vectors for consistent arrow scaling.
f) Visualize the field:
Use quiver() or streamplot() to depict vector flow,
Color arrows using $E_{magnitude}$ for intensity—highlighting hotspots and field gradients.
g) Highlight critical areas:
Overlay points where:

$$E_{magnitude}\geq E_{corona} \quad (12)$$

where,
E_{corona} is the minimum field strength required to trigger ionization (corona discharge).
These regions inform where geometric smoothing or material changes are necessary to avoid arcing.

3.2 Stage 2: Discharge physics

3.2.1 Breakdown voltage for townsend discharge

Townsend discharge defined as:

$$U_{\text{breakdown Townsend}}=\frac{d\cdot E_I}{e\cdot\lambda_e\ln\left(\frac{d}{\lambda_e}\right)} \quad (13)$$

where,
$U_{\text{breakdown Townsend}}$ is the minimum voltage to initiate breakdown in gas via electron avalanche,
d is the inter-electrode gap distance (m),
E_I is the ionization energy of the working gas (eV),
λ_e is the electron mean free path in the gas (m),
e is Euler's number (≈2.718), the base of natural logarithms.
This equation is vital for determining electrode spacing and applied voltage needed to initiate discharge reliably under given atmospheric conditions. The experimental implementation shown in 3 validates these theoretical predictions, demonstrating successful discharge initiation and measurable thrust generation.

$$L=\frac{k_BT}{\pi r_I^2} \quad (14)$$

where,
L is the mean free path of gas ions (m),
k_B=1.38×10^{-23} J/K is the Boltzmann constant,
T is the absolute temperature of the gas in Kelvin,
r_I is the ionic radius of the gas molecule (m).
This relationship aids in selecting appropriate working gases and predicting discharge uniformity across operating temperatures.

3.2.2 High voltage generation circuits

Two main circuit topologies were considered:
ZVS (Zero Voltage Switching) Circuit,[11] used for efficient low-noise voltage stepping without hard-switching losses.
Marx Generator,[12] used for generating high-voltage pulses by charging capacitors in parallel and discharging them in series—suitable for impulse or burst-mode operations.

3.3 Stage 3: Material selection

3.3.1 Electrode materials

Aluminum is considered due to its relatively high electrical conductivity, approximately 3.5×10^7 S/m. However, it is prone to oxidation, which reduces conductivity over time, especially in high-voltage environments. From a fabrication standpoint, aluminum is easy to machine and can be cast or extruded into a variety of shapes. Nevertheless, the formation of non-conductive aluminum oxide layers requires mechanical or chemical removal prior to deployment. To mitigate this issue, surface treatments such as electroplating, anodizing, or the application of oxidation-resistant coatings (e.g., silicone-based varnishes) are typically employed to preserve conductivity and protect against environmental degradation.

3D printing emerges as an alternative method for producing custom electrode geometries. Conductive filaments, including carbon-filled composites like graphene or carbon nanotubes, and metallic filaments such as stainless steel or titanium, can be used to achieve acceptable levels of conductivity. This approach is especially advantageous when complex geometries such as non-planar or hollow structures are needed, allowing the designer to tailor the electrode profile to minimize ion wastage and optimize field shaping.

3.3.2 Surface conversion to conductive

To enhance the conductivity of base materials, electroplating is widely employed. Silver plating, with a typical thickness of 5–10 μm, offers minimal resistance and remains stable under high-voltage conditions, making it suitable for precision applications. Nickel plating is often chosen in harsher operational environments due to its superior corrosion resistance and good electrical performance under high-voltage stress. Copper plating is more cost-effective and readily available, making it suitable for low-to-medium power applications. However, copper is prone to oxidation and may require additional protective coatings for long-term durability.

The electroplating procedure begins with surface preparation, typically involving solvent cleaning with agents such as acetone to remove any oils, grease, or contaminants. An activation step follows, where a dilute acid like HCl is applied to promote surface readiness for plating. The electrode is then immersed into a plating solution containing the desired metal ions (e.g., copper, nickel, or silver), and a constant current density, typically ranging between 1–10 A/dm², is applied. This ensures uniform deposition and strong adhesion of the plated layer to the substrate.

3.4 Stage 4: Electrode geometry optimization

3.4.1 Modeling the 3D Geometry to minimize ion wastage

The optimization of electrode geometry begins with simulation tools, particularly those based on the Finite Element Method (FEM). Using solvers such as COMSOL Multiphysics, one can accurately simulate the electric field distribution around the negative electrode. These simulations help to identify regions of field divergence where ion trajectories may deviate from the intended direction. The electrode shape is then adjusted to minimize sharp edges and maintain a concave profile that guides ions directly toward the positive electrode. This geometric refinement reduces regions prone to unwanted corona discharge and enhances ion throughput.

In addition to initial simulations, FEM solvers are used to conduct Finite Element Analysis (FEA) for optimizing the electric potential across the electrode surface. The primary

objective is to eliminate localized electric field spikes, which can result in ion wastage or unintended discharges. To accomplish this, the meshing density is increased in regions exhibiting high electric field gradients while remaining coarse in areas of lower significance. This ensures computational efficiency while preserving accuracy in critical zones. The comparative analysis between closed electrode profiles (Fig. 5) and open curved configurations (Fig. 6) illustrates how simulation results directly inform optimal geometry selection for maximum ion throughput.

3.4.2 Modular design for efficient ion flow

A modular approach to electrode geometry allows for easy adaptation and experimental testing. Modular sections should be interchangeable, enabling the evaluation of different geometrical configurations such as cylindrical, parabolic, or other custom shapes. These modules must include mounting mechanisms such as threaded inserts or integrated joints to maintain structural integrity during operation. This modularity provides the flexibility to tune field behavior and ion flow paths for maximum efficiency.

For thorough validation, each electrode module should include interchangeable side features to investigate ion losses at the periphery. These features might include wing-like extensions, grooves, or tapered shapes designed to suppress side ion escape. A dedicated swapping mechanism is recommended, ensuring that geometry changes can be implemented without disturbing the alignment or configuration of the remaining system. This guarantees repeatability and control over each test variable during experimental evaluations.

3.5 Stage 5: System integration

3.5.1 Skeletal hub design

The skeletal hub, acting as the structural backbone of the propulsion system, must be rigid, lightweight, and thermally stable. Composite materials such as carbon-fiber-infused PLA, produced via 3D printing, offer an ideal balance of strength and manufacturability. The hub should include provisions for adjustability, such as customizable slots and mounting rails, allowing it to accommodate a variety of electrode modules and experimental setups.

Functionally, the hub must ensure precise mechanical alignment of the electrodes, preserving the optimal gap distance required for efficient ion acceleration and uniform field distribution. It should incorporate features like adjustable mounts, quick-release mechanisms for fast geometry changes, and reinforced channels for secure cable management. These elements collectively contribute to the robustness and adaptability of the system.

3.5.2 Hub modularity and scalability

To enhance functionality, the hub should be designed with embedded slots and compartments for additional components such as high-voltage power supplies, sensors for monitoring voltage, temperature, and ionization levels, and passive or active capacitors for voltage regulation. Diagnostic tools like oscilloscopes and ammeters can also be integrated within these provisions for real-time system monitoring.

Moreover, the hub should support rapid reconfiguration to test various electrode geometries or scale up the system. A modular attachment system allows users to expand or adapt the architecture for different experimental regimes, accommodating increased electrode counts, altered voltages, or alternative propulsion test parameters. This scalability ensures the design remains applicable across both low-power micro-thrusters and larger, more demanding configurations.

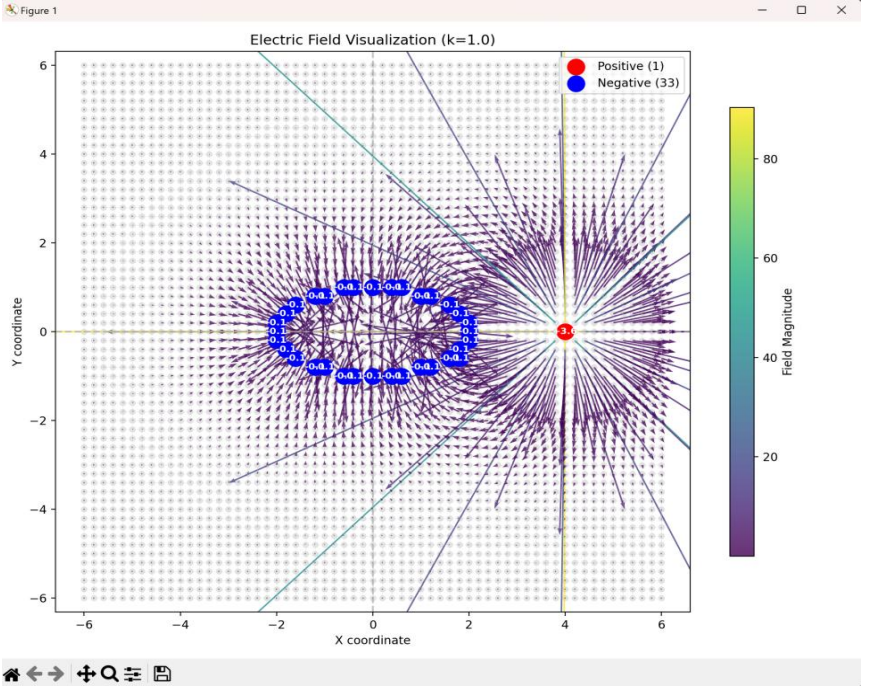

Fig. 5: Point charge behaving with negative ellipse profile.

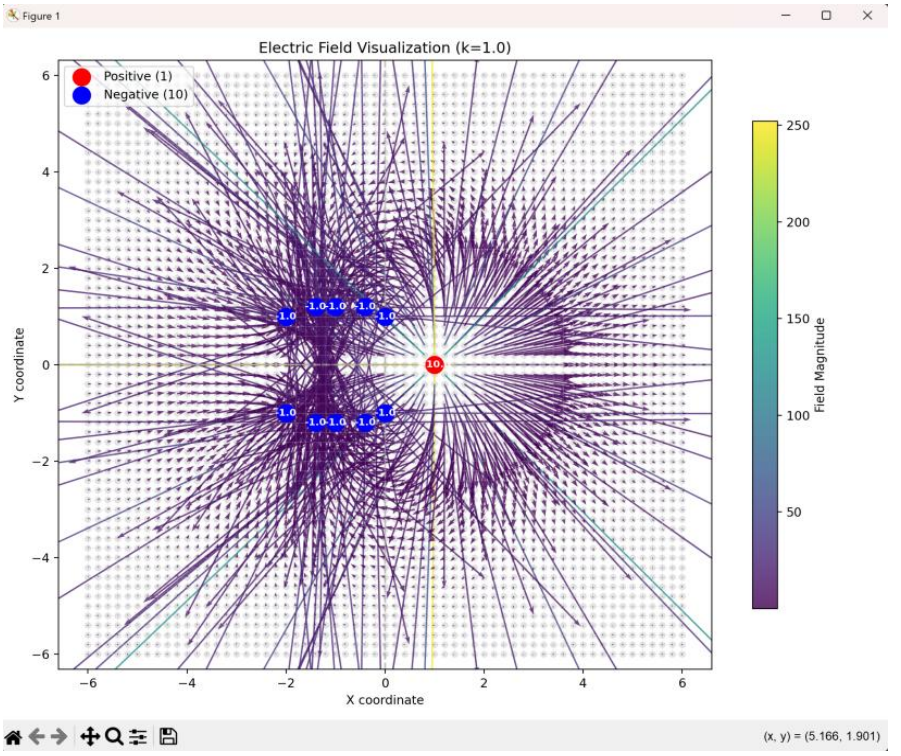

Fig. 6: Point charge behaving with two curved slabs.

4. Results

Multiple experimental iterations were carried out to assess the viability, efficiency, and directional stability of the proposed open-system ionic thruster. The initial prototype was tested with a basic electrode configuration and no shielding or enclosure. During this test, the system produced approximately 2.35 mN of thrust, recorded as a 0.24 g upward force on a precision scale, as seen in the experimental data in Fig. 3. This result verified initial ion acceleration and directional ejection under laboratory conditions. Upon refining the electrode geometry, surface treatment, and electrode alignment, a second iteration was developed, shown in Fig. 1 and Fig. 2. This improved setup demonstrated an enhanced thrust output of up to 5 mN. The increase in performance can be attributed to reduced ion recombination and more directed field lines due to geometric enhancements. However, as evident from field observation and mass measurements, a significant portion of thrust was lost sideways. This loss primarily resulted from the absence of side enclosures and electromagnetic shielding, which allowed the ion stream to diffuse laterally rather than remaining collimated in the intended axial direction. Limitations in material availability restricted the achievable precision in electrode shaping. Consequently, the optimized geometry was still sub-optimal in terms of beam guidance and thrust-vector focus. Figs. 1 and 2 depict the final form of the iterated design, where improved shaping of the negative collector helped confine ion trajectories, though further improvement is needed for ideal confinement. The effective range of ion acceleration was also investigated. Ion diffusion was observed to dominate after approximately 40 cm–50 cm of axial travel. Beyond this point, thrust efficiency dropped significantly, indicating the lack of beam confinement or collimation—a problem that could be mitigated in future models by adding magnetic or electrostatic lensing. Fig. 4 presents the first electrode modification test, showcasing the early design phase that informed the more efficient iterated models.

As in the basic simulation results it's evident that the ion thruster provides more thrust with converging or diverging tubes Fig. 6 rather than closed structures Fig. 5 and also diffuses more and has field losses more in open structures (Fig. 6).

5. Conclusion

The development of the open-system ionic thruster presented in this work demonstrates a promising advancement toward silent, efficient, and mechanically minimal propulsion under atmospheric conditions. By emphasizing the shaping of the negative collector electrode to control electric field topology, the system eliminates the need for magnetic confinement while maintaining directional ion acceleration. Experimental iterations confirmed thrust generation up to 5 mN, validating the viability of electrostatic-only ion propulsion using ambient air as the working medium. The observed lateral ion losses and limited confinement beyond 50 cm indicate the need for improvements in plume collimation and side shielding, which form the basis for future refinements.

The modular and scalable nature of the design-achieved without moving parts—offers significant potential for integration into low-noise aerial platforms such as UAVs, stealth drones, and high-altitude vehicles. Furthermore, the

ease of adapting electrode geometries and power supply configurations opens avenues for tailoring performance to mission-specific requirements. Future work will focus on addressing observed limitations by incorporating side enclosures, refining electrode fabrication with better materials, and enhancing power electronics. With further optimization and system integration, this technology could contribute meaningfully to the advancement of next-generation aerospace propulsion systems.

Conflict of Interest

There is no conflict of interest.

Supporting Information

Not applicable.

Use of artificial intelligence (AI)-assisted technology for manuscript preparation

The authors confirm that there was no use of artificial intelligence (AI)-assisted technology for assisting in the writing or editing of the manuscript and no images were manipulated using AI.

References

[1] H. Xu, Y. He, K. L. Strobel, C. K. Gilmore, S. P. Kelley, C. C. Hennick, T. Sebastian, M. R. Woolston, D. J. Perreault, S. R. H. Barrett, Development of advanced high-temperature propulsion materials, *Nature*, 2018, **563**, 354-23 NM,59, doi: 10.1038/s41586-018-0707-9.

[2] D. M. Goebel, I. Katz, Fundamentals of electric propulsion: ion and hall thrusters, JPL Space Science and Technology Series, NASA Jet Propulsion Laboratory, Pasadena, CA, 2008, available: https://descanso.jpl.nasa.gov/SciTechBook/series1/Goebel__cmprsd_opt.pdf.

[3] H. Kamhawi, W. Huang, T. Haag, R. Shastry, R. Thomas, J. Yim, D. Herman, G. Williams, J. Myers, R. Hofer, I. Mikellides, M. Sekerak, J. Polk, Performance and facility background pressure characterization tests of NASA's 12.5-kW hall effect rocket with magnetic shielding thruster, Joint Conference of 30th ISTS, 34th IEPC and 6th NSAT, Kobe-Hyogo, Japan, July 4 – 10, NASA Technical Reports, 2015.

[4] Indian Space Research Organization, ISRO successfully completes 1000hrs life test of stationary plasma thruster for spacecraft electric propulsion system, ISRO Press Release, March 27, 2025, available: https://www.isro.gov.in/ISRO_successfully_conducts_1000hrs_life_test_of_SPT.html.

[5] Busek Co. Inc., Hall Thrusters - BHT Series, Busek Company Technical Specifications, accessed 2024, https://www.busek.com/hall-thrusters.

[6] SETS Space, Xenon, krypton, or argon propellants for hall thruster efficiency: properties, applications, and cost, 2023, available at: https://sets.space/xenon-krypton-or-argon-propellants-for-hall-thruster-efficiency-properties-applications-and-cost/.

[7] J. Jackson, M. Allen, R. Myers, E. Soendker, B. Welander, A. Tolentino, C. Sheehan, J. Cardin, J. S. Snyder, R. R. Hofer, T. A. Tofil, and D. A. Herman, 13 kW Advanced electric propulsion flight system development and qualification, 2019 International Electric Propulsion Conference, *V*ienna, Austria, 2019, available: https://ntrs.nasa.gov/api/citations/20190032202/downloads/20190032202.pdf.

[8] R. J. Cassady, S. Wiley, J. Jackson, A. Rocketdyne, Status of advanced electric propulsion systems for exploration missions, 69th International Astronautical Congress, Bremen, Germany, 2018, available: https://www.researchgate.net/publication/328997773_Status_of_Advanced_Electric_Propulsion_Systems_for_Exploration_Missions.

[9] Frore Systems, AirJet: the world's first solid-state active cooling chip, 2023, available at: https://www.froresystems.com/technology/.

[10] Frore Systems, AirJet® Mini Slim removes 5.25 Watts of heat at a silent 21 dBA noise level, Frore Systems, 2024, available: https://www.froresystems.com/products/airjet-r-mini-slim

[11] S. Kathole, R. Rooge, N. Bharambe, ZVS circuit based – Cockcroft Walton high voltage dc generator, *International Research Journal of Engineering and Technology,* 2022, **9**, 1–6.

[12] K. J. Chung, Marx generators and Marx-like circuits, Department of Nuclear Engineering, Seoul National University, 2018.